nature communications

Article | Article in Press

https://doi.org/10.1038/s41467-026-79186-1

A motion vector sensor-enabled 3D spinal morphology monitoring suit for intelligent scoliosis identification

Received: 16 April 2026

Accepted: 14 October 2026

Published online: 30 October 2026

Check for updates

Liangxu Xu[1,2,3,11], Guilin Chen[4,5,11], Hongjun Liu[6,11], Xuan Zhao[1,2,3,11], Chao Yao[6], Haonan Si[1,2,3], Mao Lin[7], Yu Wang[8], Bingwu Wang[9], Xiangjie Yin[4,5], Jing Yuan[10], Guixing Qiu[4,5], Zhihong Wu[4,5], Terry Jianguo Zhang[4,5] ✉, Qingliang Liao[1,2,3] ✉, Yue Zhang[1,2,3] ✉ & Nan Wu[4,5] ✉

Early identification of scoliosis is important for timely clinical intervention. However, conventional static screening methods rely on subjective assessments, resulting in limited accuracy and insufficient continuity. Here, we propose a motion vector sensor-enabled 3D spinal morphology monitoring suit for intelligent scoliosis identification. We engineer a highly anisotropic mesh with orderly aligned conductive fibers, enabling the motion sensors to precisely perceive motion amplitude and direction. The suit integrates motion sensors positioned at symmetrical body locations to quantify 3D spinal motions bz capturing skin-surface deformation amplitude and direction. We achieve dynamic scoliosis identification through machine learning-powered evaluation of spinal kinematic symmetry. We test performance on a multi-center cohort comprising four hospitals and one school-based screening program, demonstrating 92.63%, 71.05%, and 82.76% accuracy for scoliosis detection, curvature degree quantification, and curvature location identification, respectively. This radiation-free alternative has the potential to support longitudinal follow-up and reduce repeat radiographs in scoliosis management.

Scoliosis is clinically defined as a lateral curvature exceeding 10° according to the Cobb angle measurement and is often accompanied by 3D spinal deformity associated with misalignment in the coronal, sagittal, and axial planes[1]. Scoliosis worsens over time, leading to significant changes in body morphology, such as asymmetrical shoulder height, deviation of the spine from the midline, and the development of a rib hump deformity[2,3]. Furthermore, excessive spinal curvature may lead to a variety of complications, such as neck pain, shoulder discomfort, lower back pain, paralysis, and cardiorespiratory dysfunction, potentially increasing the risk of mortality[4–6]. To date, surgery remains the only effective intervention for correcting severe curvatures, despite its association with substantial trauma and reduced spinal mobility. In the early stages of scoliosis, spinal curvature is typically mild, and external deformities remain inconspicuous, hindering the timely detection of disease onset[7,8]. Given that early-stage scoliosis often goes undetected, systematic screening plays a crucial role in facilitating early identification of the disease. Early identification and timely intervention constitute essential components of effective disease management[9].

Traditional approaches for early scoliosis identification include the forward bend test (FBT), Scoliometer, and Moiré topography, with disease confirmation achieved through X-ray examination in suspected patients[10–14]. The reported accuracy of conventional screening depends strongly on the combination of tests used: in the most recent systematic review, the FBT alone achieved a sensitivity of 84.4%, the FBT combined with scoliometer measurement achieved a sensitivity of

A full list of affiliations appears at the end of the paper. jgzhang_pumch@yahoo.com; liao@ustb.edu.cn; yuezhang@ustb.edu.cn; dr.wunan@pumch.cn

71.1% and a specificity of 97.1%, and the combination of FBT, scoliometer and Moire topography achieved a sensitivity of 93.8% with regular screening, with a 95% confidence interval (CI) of 93.3–94.3%, and a specificity of 99.2%[15]. All of these protocols are static, single-timepoint assessments that depend on the examiner's subjective judgment, and the more accurate combinations require equipment and training that are not available in most school-based screening programs. This inherent limitation may compromise the feasibility of timely follow-up assessments during scoliosis treatment and correction—particularly in adolescents experiencing rapid skeletal growth. Throughout this work, screening refers to the identification, within a population that has not undergone radiographic assessment, of individuals who should be referred for radiography, whereas diagnosis refers to the radiographic confirmation of a Cobb angle of 10° or greater, which remains the clinical reference standard. The system described here is designed to operate at the screening and follow-up stage, with the aim of reducing the number of confirmatory and repeat radiographs rather than replacing them.

Patients with scoliosis exhibit a diminished range of spinal movement and a significant increase in postural asymmetry when performing symmetrical movements along the sagittal, coronal, and transverse planes[16–18]. The kinematic symmetry evaluation of the spine serves as a promising approach to enable the early detection and continuous monitoring of scoliosis. Compared with conventional optical motion capture systems and inertial measurement units[19–22], body-worn flexible motion sensors enable direct, contact-based electromechanical transduction, thereby perceiving human movement with high fidelity, free from spatial limitations and electromagnetic interference[23–27]. These characteristics make them highly promising for use in the kinematic symmetry assessment of the spine. Moreover, the motion sensors can dynamically perceive spinal movements over a long time period, yielding spinal health assessments that are more continuous and comprehensive compared to traditional single-time static measurements[28–31]. However, most existing motion sensors face a significant challenge: they are only capable of detecting uniaxial tensile amplitude but fail to recognize tensile direction[32–35]. This limitation arises from the isotropic sensitive layers, which tend to respond indiscriminately to stretching in any direction[36–39]. The spine, endowed with numerous articulations and degrees of freedom, exhibits complex motion modes with various amplitudes, directions, and postures. These sensors are incapable of perceiving 3D spinal movements with multiple degrees of freedom, thereby significantly obstructing the precise and comprehensive kinematic symmetry evaluation of the spine.

Here, we propose a motion vector sensor-enabled 3D spinal morphology monitoring suit for intelligent identification and quantitative assessment of scoliosis. The motion vector sensors are fabricated by orthogonally stacking two anisotropic conductive meshes, which achieves fine quantification of motion amplitude and direction with the assistance of the heterogeneous strain distribution. The sensors achieve a minimum directional resolution of 2° and a linear working range up to 100% strain. Furthermore, a 3D spinal morphology monitoring suit with embedded motion sensors at symmetrical body locations is integrated to enable real-time tracking of 3D spinal motions by precisely detecting the amplitude and direction of skin deformation. Dynamic scoliosis identification is achieved by assessing the symmetry of human postures during symmetrical 3D spinal motions with the assistance of artificial intelligence. The accuracy rates for scoliosis detection, curvature degree quantification, and curvature location identification are 92.63%, 71.05%, and 82.76%, respectively. This work presents a feasible alternative for radiation-free scoliosis screening, with the potential to support longitudinal follow-up and to reduce the number of repeat radiographs required during the management of the condition.

Results

Design concept and methodology of the motion vector sensor-enabled 3D spinal morphology monitoring suit

Located centrally along the human body's longitudinal axis, the spine serves as the most essential structure for providing support and maintaining balance in the human body. Under the traction of numerous muscles, movement between multiple vertebrae cooperatively enables the spine to complete complex 3D motions, such as flexion, extension, lateral flexion, and rotation. Simultaneously, the 3D motions of the spine induce alterations in human posture and body surface morphology. Spinal motion X-rays demonstrate that in a healthy individual, the sequential performance of three sets of symmetrical spinal motions—flexion and extension, left and right lateral flexion, and left and right rotation—results in correspondingly symmetrical postural changes (Fig. 1a and Supplementary Movie S1). Consequently, under symmetric spinal motions, the amplitude and direction of skin deformation at symmetrical positions will be approximately consistent due to postural changes. However, in patients with scoliosis, body symmetry is significantly reduced as a result of the distorted spinal morphology (Fig. 1b and Supplementary Movie S2). Thus, postural symmetry during each set of spinal motions is also diminished, leading to substantial differences in both the direction and amplitude of skin deformation at symmetrical positions. Furthermore, the alterations in body surface morphology at symmetrical positions vary among patients with thoracic or lumbar curvature during symmetrical spinal motions (Supplementary Fig. S1). Therefore, it should be feasible to screen for scoliosis and to assess curve severity by assessing the symmetry of human postures during symmetrical spinal motions.

Toward this goal, a 3D spinal morphology monitoring suit with embedded motion sensors is proposed for radiation-free screening and longitudinal assessment of scoliosis. As illustrated in Fig. 1c, two types of motion sensors, including the uniaxial motion sensor and motion vector sensor, are placed at symmetrical body positions and function collaboratively to track the 3D motions of the spine by detecting alterations in body surface morphology. When the wearer performs three sets of symmetrical motions in sequence, the monitoring signals that reflect changes in body surface morphology can be recorded and transmitted to the intelligent terminal by the custom-made flexible printed circuit board (FPCB). The symmetry of postural motion can be effectively assessed based on the consistency of skin deformation data, which can be utilized to identify scoliosis and quantify its severity.

The motion vector sensor comprises a top encapsulation layer, a top strip-shaped sensing layer, an insulating layer, a bottom strip-shaped sensing layer, and a bottom encapsulation layer, with the top and bottom sensing layers orthogonally aligned (Fig. 1d). Within this architecture, the anisotropic elastomer mesh based on unidirectional alignment fibers serves as the sensitive layer, enabling the device to perceive motion amplitude and direction simultaneously. The uniaxial motion sensor consists of sandwiching two encapsulation layers with a strain-sensitive layer, which can linearly respond to tensile strains in a specific direction (Supplementary Fig. S2). The anisotropic polyurethane (PU) mesh is fabricated via a precisely controlled electrospinning process, with fiber alignment modulated through joint adjustment by both stress and voltage fields (Fig. 1e and Supplementary Fig. S3a, b). Subsequent ultrasonic-assisted dip-coating with carbon nanotubes (CNTs) yields the anisotropic CNTs@PU mesh (Supplementary Fig. S3c, d). This composite mesh retains robust electrical conductivity even under large uniaxial tensile strain (Supplementary Fig. S3e). The CNTs@PU fibers are continuous and morphologically uniform, with preferential orientation aligned closely with the 90° axis (Fig. 1f and Supplementary Fig. S4). Furthermore, CNTs conformally coated on the PU fiber surfaces overlap extensively,

https://doi.org/10.1038/s41467-026-79186-1

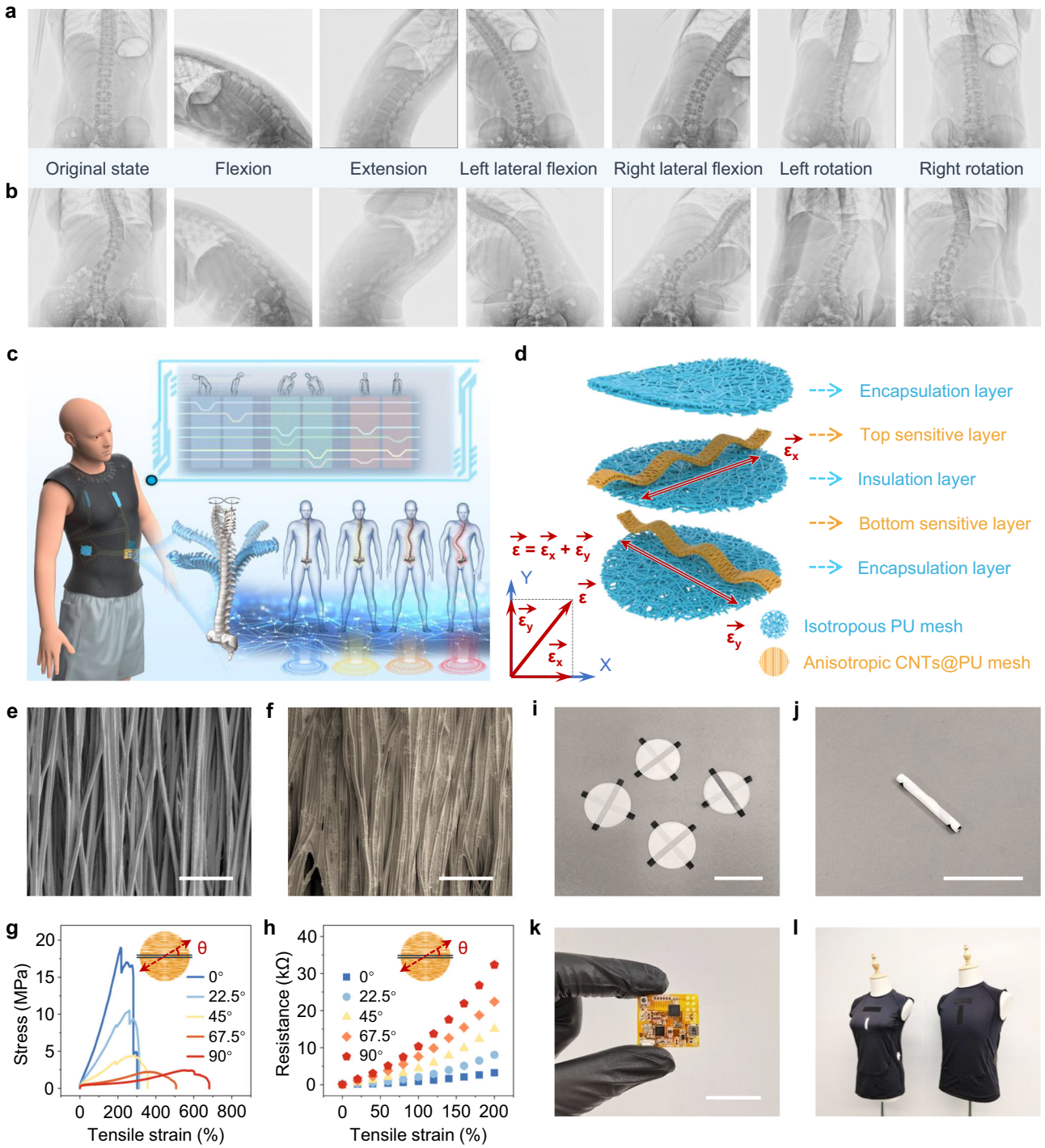


Fig. 1 | Design concept and methodology of the motion vector sensor-enabled 3D spinal morphology monitoring suit. a, **b** X-ray images of a healthy person (**a**) and a patient with scoliosis (**b**) when performing three sets of symmetrical motions of the spine, including flexion, extension, left lateral flexion, right lateral flexion, left rotation, and right rotation. **c** Schematic diagram of the motion vector sensor-enabled 3D spinal morphology monitoring suit for intelligent scoliosis screening. **d** Schematic structure diagram of the motion vector sensor. ε_x and ε_y are the component vectors along the X-axis and Y-axis, respectively, and ε is the resultant vector. **e** Scanning electron microscopy (SEM) image of polyurethane (PU) mesh based on unidirectionally aligned fibers. Three times experiment was repeated independently with similar results. Scale bar: 20 μm. **f** SEM image of the PU mesh with carbon nanotubes (CNTs@PU mesh) based on unidirectionally aligned fibers. Three times experiment was repeated independently with similar results. Scale bar: 20 μm. **g** Stress–strain curves of the CNTs@PU mesh along different tensile directions. θ is defined as the angle between the baseline and the tensile direction. **h** Resistance changes of the CNTs@PU mesh versus applied tensile strains along different directions. **i** Photographic image of the motion vector sensors. Scale bar: 2 cm. **j** Optical image of the motion vector sensors when rolled up. Scale bar: 4 cm. **k** Photographic image of the custom-made flexible printed circuit board (FPCB), which can be used for portable acquisition and wireless transmission of multi-channel signals. Scale bar: 2 cm. **l** Photographic image of the motion vector sensor-enabled 3D spinal morphology monitoring suit.

establishing a percolating, 3D conductive network (Supplementary Fig. S5).

Figure 1g, h presents the stress-strain curves and corresponding resistance changes of the unidirectional alignment CNTs@PU fibers under uniaxial stretching along various directions. Supplementary Fig. S6 illustrates the morphological evolution of the same material during deformation. Collectively, these results demonstrate that the electromechanical behavior of the CNTs@PU mesh is markedly anisotropic. A high tensile modulus of 8.77 MPa is measured when the CNTs@PU mesh is stretched parallel to the fiber orientation ($\theta = 0°$), as intrinsic elastic deformation dominates during stretching. Consequently, nanoscale crack nucleation occurs without significant propagation, yielding a gradual resistance increase to 3.23 kΩ. In contrast, a minor tensile modulus of 0.35 MPa is observed when the mesh is stretched perpendicular to the fiber direction ($\theta = 90°$), where deformation arises predominantly from inter-fiber sliding, buckling, and macroscopic structural reorganization. This leads to extensive micron-scale crack migration across the network, resulting in a rapid increase in its resistance to 32.36 kΩ. Varying the tensile direction enables effective modulation of the relative contributions of intrinsic elastic deformation and structural reorganization within the CNTs@PU mesh, thereby governing crack initiation, morphology, and spatial distribution and ultimately giving rise to pronounced anisotropy in its electromechanical response. An unordered-fiber-based PU mesh is also fabricated to serve as the encapsulating and insulating layer, and mechanical characterization confirms its pronounced isotropic behavior (Supplementary Fig. S7).

Both the PU mesh and the CNTs@PU mesh are thermoplastic materials. Leveraging their excellent thermal formability, the motion vector sensors are constructed via the hot-pressing process, and their optical image is shown in Fig. 1i. Under the optimal hot-pressing conditions, the fiber interfaces between the PU mesh and the CNTs@PU mesh undergo a localized melting and bonding process, resulting in robust interfacial bonding analogous to thermal welding (Supplementary Fig. S8a). The bonding strength between the PU mesh and the CNTs@PU mesh increases progressively with rising hot-pressing temperature, applied pressure, and dwell time (Supplementary Fig. S8b). The optimal hot-pressing parameters included a pressure of 10 MPa, a temperature of 60 °C, and a duration of 30 s, and the sensor surface was white and retained its fiber structure (Supplementary Fig. S8c–e). In contrast, high hot-pressing temperature, excessive applied pressure, or prolonged dwell time will damage its intrinsic fiber architecture (Supplementary Fig. S8f). The robust interfacial bonding within the multilayered architecture can withstand substantial in-plane interfacial shear stresses arising from strain mismatches, thereby preventing delamination between functional layers under repetitive or excessive mechanical deformation (Supplementary Fig. S9). The motion vector sensor can also be easily rolled up, demonstrating its desirable softness and conformability (Fig. 1j).

Figure 1k and Supplementary Fig. S10 exhibit the optical image and circuit diagram of the custom-made FPCB, which can achieve multi-channel signal acquisition and wireless transmission of the spinal motion signals. The 3D spinal morphology monitoring suits are further prepared through the integration of hardware and software (Fig. 1l). To achieve highly robust electrical connections between the strain-sensitive layer and interconnection lines, conductive silver paste and soft fabric are further employed to mechanically reinforce and fully encapsulate the electrical interface (Supplementary Fig. S11 and Note S1). We also considered the inter-individual differences in body mass index (BMI) and sex-specific torso morphology in the design of the wearable suit. Five standardized sizes (S, M, L, XL, and 2XL) were developed. The participants can scientifically match appropriate sizes based on anthropometric parameters such as height, weight, chest circumference, and waist circumference to ensure conformal attachment to the skin surface, thereby enhancing the accuracy of directional and amplitude-resolved quantification of skin deformation.

Working mechanism and sensing performance of the motion vector sensor

Figure 2a shows the schematic diagram of the motion vector sensor under uniaxial tensile loading at varying orientations, where θ is defined as the angle between the baseline and the tensile direction. Figure 2b and Supplementary Fig. S12 show the simulation results for stress concentration and strain distribution, respectively, revealing that heterogeneous strain distributions emerge within the device as stretch directions are changed. Under uniaxial stretching along the 0° direction, the top-sensitive layer exhibits a high tensile modulus, enabling it to resist tensile deformation and thereby divert mechanical load predominantly to the low-modulus encapsulation and insulation layers. Even under 100% tensile strain applied at 0°, the top-sensitive layer exhibits minimal nanoscale crack formation (Fig. 2c and Supplementary Fig. S13a), and its relative resistance change hardly fluctuates (Supplementary Fig. S14b). As θ increases from 0° to 90°, the tensile modulus of the top-sensitive layer gradually decreases, while its tensile deformation increases correspondingly. Under uniaxial stretching along the 90° direction, the top-sensitive layer performs a tensile modulus closely matched to that of the encapsulation and insulation layers, resulting in consistent deformation. Micron-scale crack generation and migration induce the resistance to rapidly increase to its maximum value (Fig. 2c, Supplementary Fig. S13b and Supplementary Fig. S14f). In contrast, the tensile modulus of the bottom-sensitive layer gradually enhances with the increase in θ. Correspondingly, its relative resistance change reaches its maximum at $\theta = 0°$ and declines to a minimum at $\theta = 90°$ (Supplementary Fig. S14).

Figure 2d presents the dynamic resistance response of the top-sensitive layer under cyclic tensile loading at 100% strain across directions from 0° to 90°. As θ increases, the tensile morphology of the top-sensitive layer gradually transitions from nanoscale crack propagation to the microscale interlaced network migration, resulting in a stepwise increase in the electromechanical response amplitude. As expected, the bottom-sensitive layer exhibits a stepwise decrease in dynamic resistance response under identical loading conditions (Fig. 2e). The peak relative resistance change reaches its maximum under uniaxial tensile loading at $\theta = 90°$ for the top-sensitive layer and at $\theta = 0°$ for the bottom-sensitive layer. 2D mapping results of the top- and bottom-sensitive layers are generated according to the amplitudes and directions of applied tensile strain, as well as the corresponding peak relative resistance change, as presented in Fig. 2f, g. These results provide a quantitative, visual representation of the anisotropic coupling between mechanical input and electrical output, thereby directly linking directional strain input to its corresponding electrical output.

Under identical deformation conditions, the response signal of the strain-sensitive layer is jointly determined by both the amplitude and direction of the applied tensile strain. Consequently, a motion vector sensor incorporating orthogonally aligned top- and bottom-sensitive layers can be employed to decouple and quantify both the amplitude and direction of the applied tensile strain. When the tensile strains are applied in multiple directions, the top- and bottom-sensitive layers generate specific response signals corresponding to the strain-loading conditions (Fig. 2h). Consequently, the intensities of the dual-response signals reflect both the amplitude and direction of the applied tensile strain. The motion vector sensor also demonstrates a high sensitivity to the tensile direction, reliably resolving incremental changes in tensile loading direction as small as 2° (Fig. 2i). Compared with previously reported sensors, the motion vector sensor exhibited significant advantages in two key performance characteristics: a minimum directional resolution of 2° and a linear working range up to 100% strain (Supplementary Table S1).

https://doi.org/10.1038/s41467-026-79186-1

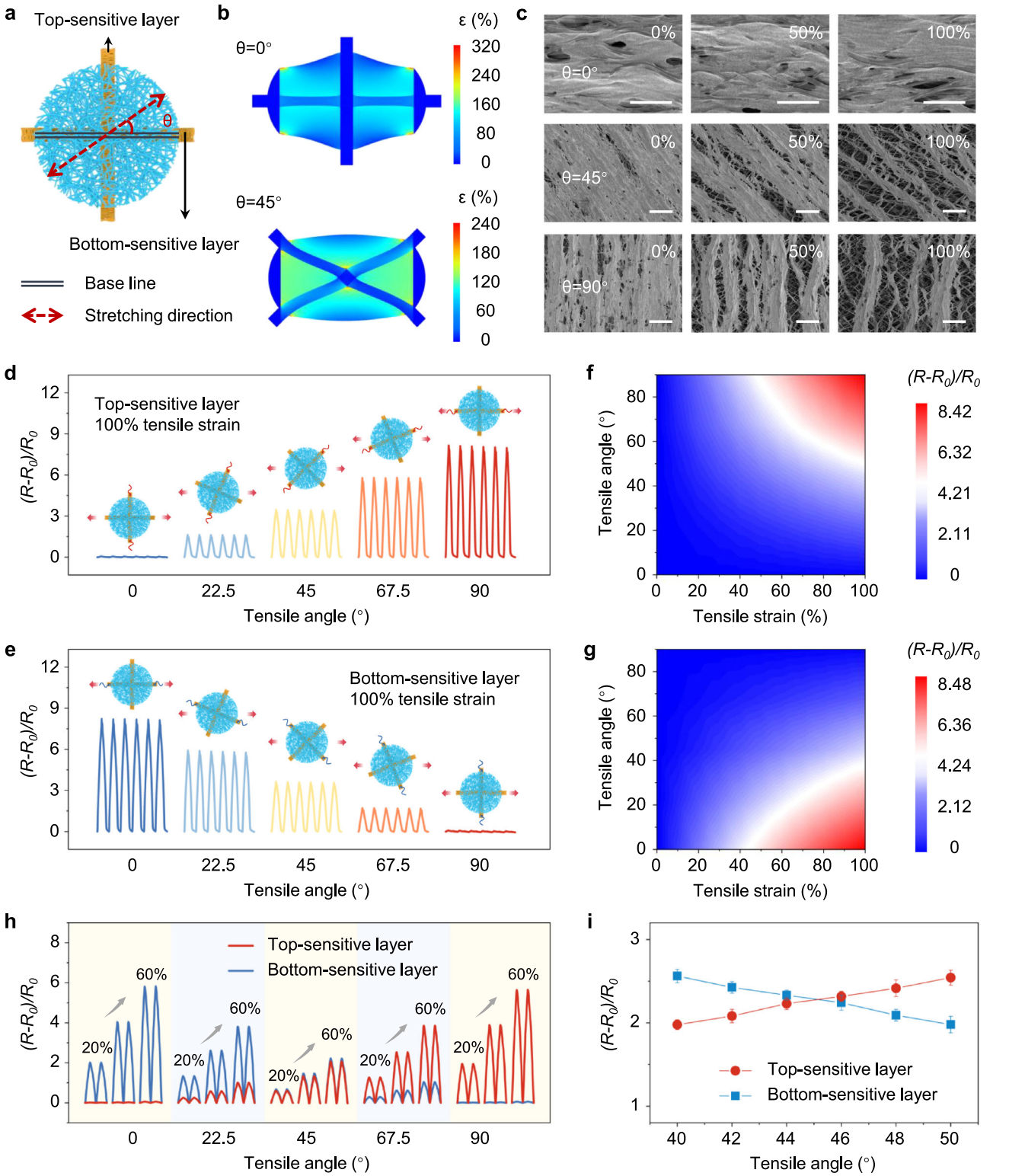


Fig. 2 | Working mechanism and sensing performance of the motion vector sensor. a Schematic illustration of the motion vector sensor when stretched along different directions. **b** Strain-distribution simulations of the motion vector sensor when stretched along different directions. **c** Morphology evolution of the top-sensitive layer when applying tensile strain with different amplitudes along 0°, 45°, and 90° directions. Three times experiment was repeated independently with similar results. Scale bars: 30 μm (0°), 100 μm (45°), and 100 μm (90°). **d**, **e** Response signals of the top-sensitive layer (**d**) and bottom-sensitive layer (**e**) under periodic loading strains of 100% at different tensile directions. **f**, **g** 2D fitting results of the relative resistance changes, tensile strains, and tensile directions of the top- sensitive layer (**f**) and bottom-sensitive layer (**g**) based on the experimental data. **h** Response signals of the motion vector sensor under different tensile strains applied in various directions. **i** Relative resistance changes of the motion vector sensor as the tensile angle is sequentially changed by 2°, with an applied tensile strain of 50%. Data are presented as mean ± SD ($n = 3$).

The motion vector sensor is capable of detecting dynamic strain loading over a frequency range from 0.25 to 4 Hz, which satisfies the demand for monitoring body motion (Supplementary Fig. S15a). When the rate of applied tensile strain is set at 400 mm/min and the applied tensile strain is 5%, the response and recovery times of the strain vector sensor are 105 and 178 ms, respectively (Supplementary Fig. S15b). Fatigue testing of the motion vector sensor reveals no significant degradation in sensing performance or delamination in device structure after 10,000 loading–unloading cycles at 80% strain, confirming its reliability and stability under prolonged mechanical loading (Supplementary Fig. S16). We randomly selected 10 motion vector sensors from multiple batches of fabricated devices and measured the initial resistance of the top- and bottom-sensitive layers and their maximum resistance change when applying 100% tensile strain, as shown in Supplementary Fig. S17. The initial resistance fluctuation of the biaxial strain sensors is less than 0.1 kΩ, and the maximum resistance change of the top- and bottom-sensitive layers after sufficient pre-stretching is less than 0.2, which indicates their desirable consistency and reproducibility. We systematically investigated the effect of the relative position between the top- and bottom-sensitive layers on the directional detection range of the sensor (Supplementary Fig. S18 and Note S2). The directional detection range is determined by the angle between the two strain-sensitive layers. Theoretically, any nonzero interlayer angle—however small—establishes a one-to-one mapping between each applied strain vector and its corresponding resistance change. However, at small interlayer angles, the resistance responses of the two layers exhibit strong convergence, leading to diminished signal distinguishability. When the layers are orthogonally arranged, their response signals show opposite trends, achieving the highest distinguishability.

The motion vector sensor is mounted on the cervical spine to enable real-time tracking of neck kinematics (Supplementary Fig. S19a). The sensor can specifically perceive 3D neck movements such as flexion, anterolateral flexion, and rotation by simultaneously monitoring both the amplitude and direction of skin strain induced by neck movement (Supplementary Fig. S19b). It autonomously decouples each neck motion vector into two orthogonal in-plane strain components; the amplitudes of the dual-axis signals quantitatively encode both motion amplitude and direction. Neck movement is performed in 2° increments across a range of 0° to 20°. The sensor demonstrates effective responsiveness to subtle angular changes (Supplementary Fig. S20). Notably, moving the neck in the direction that compresses the motion vector sensor will fail to induce the sensor to respond. This is because the strain-sensitive materials respond selectively to skin stretching. We consider that sensitive materials with Janus architecture have great potential to address this limitation. The ordered fibers with Janus architecture can be prepared by precise regulation of electrospun fiber dimensions. This may lead to a selective multifunctional response of sensors to directional bending and stretching, facilitating the tracking of the full-range motion of the joints.

Kinematic symmetry evaluation using 3D spinal morphology monitoring suit

The spine, endowed with numerous articulations and degrees of freedom, is capable of performing complex 3D motions, including flexion, extension, lateral flexion, and rotation across various planes of the human body (Fig. 3a). To accurately capture 3D spinal motions by detecting changes in body surface morphology, we systematically designed the positions of two types of sensors and established evaluation protocols for kinematic symmetry assessment based on human body mechanics (Supplementary Note S3 and Note S4). Figure 3b illustrates the mounting positions of two types of motion sensors. Uniaxial motion sensors are positioned at the lower margin of the sternum and the twelfth thoracic vertebra, as the changes in body surface morphology at these locations are relatively simple and predominantly involve sagittal-plane stretching. Conversely, the changes in body surface morphology at the intersection of the left and right rib edges with the midaxillary line are complex and diverse; therefore, motion vector sensors are positioned at these locations. These anatomical landmarks were defined and localized by experienced spine surgeons during the development of the monitoring suit, after which the sensor positions are realized in routine use simply by selecting an appropriately sized garment, so that specialist landmark identification is not required at the point of acquisition. We further designed three sets of symmetrical spinal motions for evaluation purposes, including flexion, extension, left and right lateral flexion, and left and right rotation motions (Fig. 3c). Among these symmetric motions, flexion and extension reflect spinal movements along the sagittal plane; left and right lateral flexion reflect spinal movements along the coronal plane; and left and right rotation reflect spinal movements along the transverse plane. Moreover, the selected positions enable more reliable alignment of the sensors along the main strain direction of the skin (i.e., the maximum stretch direction) during three sets of symmetrical spinal motions, thereby generating more significant and specific motion signals. We anticipate that quantitative assessment of asymmetry in these paired, motion-synchronized signals will support the detection and characterization of scoliosis.

To test this hypothesis, under the guidance of doctors, healthy individuals and patients with varying degrees of scoliosis wore a 3D spinal morphology monitoring suit and sequentially performed three sets of symmetrical evaluation motions. During these motions, the four sensors simultaneously recorded the response signals of body surface morphology that reflected 3D spinal movements. The working mechanism of the 3D spinal morphology monitoring suit and the generation of the 3D spinal motion signals are also elaborated in Supplementary Fig. S21 and Note S5. Figure 3d shows the optical and X-ray images of a healthy participant, demonstrating high symmetry and flexibility of the spine along the coronal plane. The flexion and extension of the spine cause the uniaxial motion sensors located at the lower margin of the sternum and twelfth thoracic vertebra to stretch along the sagittal plane and produce large response signals (Fig. 3h). The motion vector sensors positioned at the intersection of the left and right rib edges with the midaxillary line are arranged in an “X” configuration. During left and right lateral flexion of the spine, the top- and bottom-sensitive layers of the motion vector sensors on both sides produce similar tensile deformation along the coronal plane, yielding response signals that are approximately the same (Fig. 3h). However, left and right rotations of the spine cause the skin on both sides to be stretched along specific directions, eliciting a selective response by the top- and bottom-sensitive layers of the motion vector sensors. The signal amplitudes from the top-sensitive layer on the left motion vector sensor and the bottom-sensitive layer on the right motion vector sensor exhibit high consistency. Similarly, the response signal from the bottom-sensitive layer on the left motion vector sensor is comparable to that of the top-sensitive layer on the right motion vector sensor. These data indicate that, in the absence of scoliosis, the skin deformations caused by left and right rotation are approximately symmetrical. Thus, healthy people acquire approximately symmetrical response signals when performing three sets of spinal evaluation motions.

The directional resolution of the motion vector sensor under real-world conditions was studied (Supplementary Fig. S22). Healthy individuals sequentially performed left lateral flexion, left rotation, and right rotation of the spine. The amplitude of each spinal motion was set to 20°, with angular increments of 2° applied sequentially across all movement planes. The real-time response signal exhibits a stepwise change as the spinal motion angle increases. The motion vector sensor continuously and effectively responds to subtle movements, demonstrating its fine detection capability for spinal motion tracking. We also designed multiple alternative anatomical landmarks around the

https://doi.org/10.1038/s41467-026-79186-1

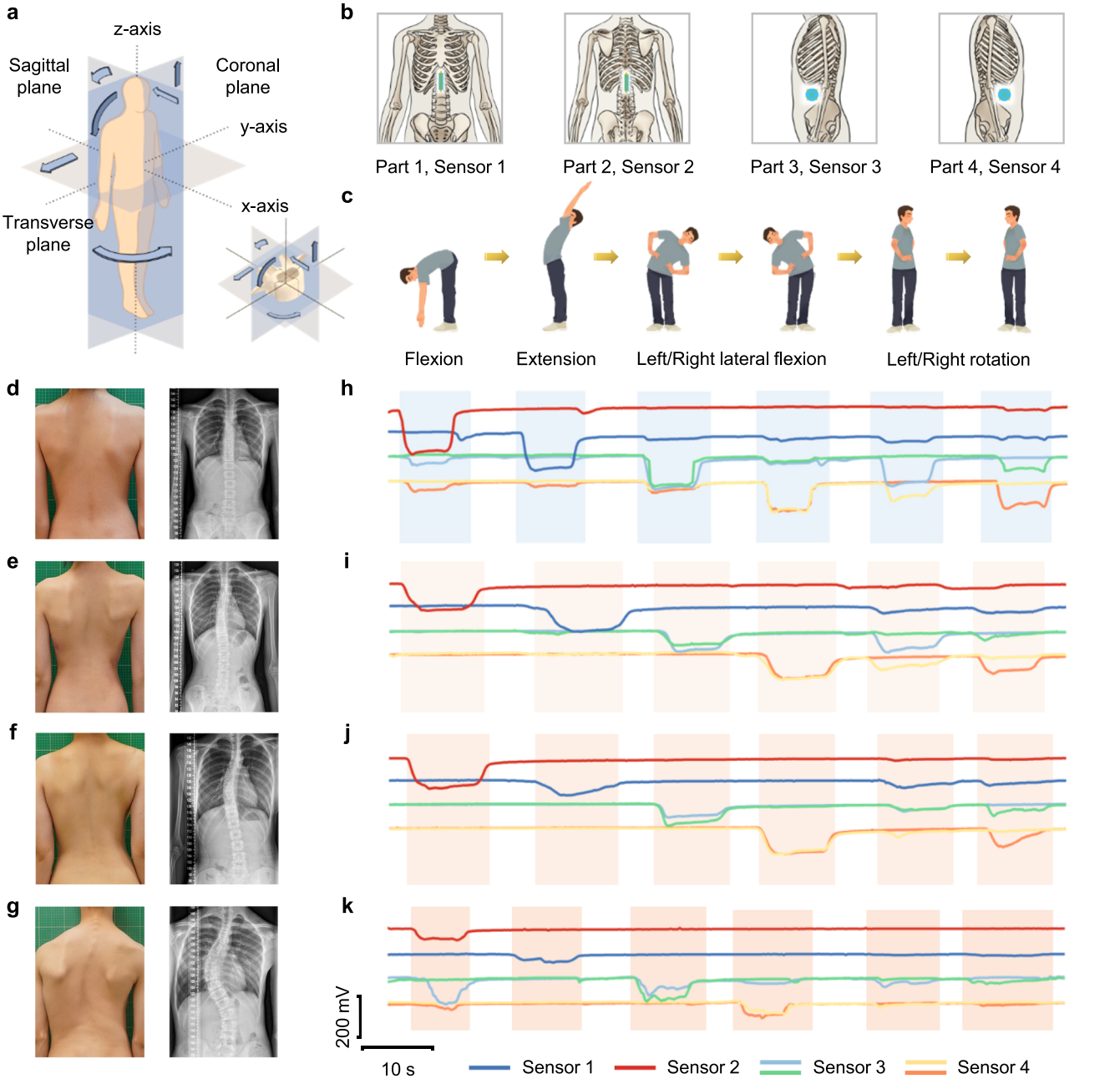


Fig. 3 | Kinematic symmetry evaluation using 3D spinal morphology monitoring suit. a The axes and planes of the human body. **b** Symmetrical wearing positions of two sets of motion sensors; sensors 1 and 2 are uniaxial motion sensors placed on the lower margin of the sternum and the twelfth thoracic vertebra, and sensors 3 and 4 are motion vector sensors placed on the intersection of the left and right rib edges with the midaxillary line. **c** Three sets of symmetrical evaluation motions of the spine. **d**–**g** Optical and X-ray images of healthy individuals and patients with varying degrees of scoliosis. **h**–**k** Real-time motion signals from healthy individuals and patients with varying degrees of scoliosis while successively performing three sets of symmetrical evaluation motions.

intended landmarks, located directly above, below, to the left, and to the right of them, with controlled offset distances, respectively (Supplementary Fig. S23–25). The intended landmarks (with an offset of 0 cm) were included as a reference control group in the analysis to establish a complete spatial deviation assessment system. When the sensor is offset along the vertical direction (up/down), the motion signal remains stable without significant fluctuations (Supplementary Figs. S23, S25b–e and S25k–n). The horizontal (left/right) offset causes the sensor to deviate from the main tensile axis direction of the skin, thereby altering the effective strain components experienced by either the top- or bottom-sensitive layer and resulting in corresponding fluctuations in signal strength (Supplementary Figs. S24, S25f–i and S25o–r). Further experimental and methodological details are provided in Supplementary Note S6. For participants with different BMIs, including underweight and overweight individuals, we achieved conformal attachment between the sensor and the skin surface by using properly sized wearable suits, thereby facilitating effective transduction of skin deformation signals into electrical signals. Experimental results demonstrate that this approach reliably captures signals with clear motion recognition across various BMIs (Supplementary Fig. S26).

In contrast to healthy individuals, scoliosis causes a significant decrease in both spinal symmetry and flexibility, resulting in inconsistent morphological changes on both sides of the body even under

symmetrical motions. Figure 3e shows the optical and X-ray images of a patient with mild scoliosis, exhibiting a thoracic Cobb angle of 15° and a lumbar Cobb angle of 14°. The signal intensities of the top- and bottom-sensitive layers in the motion vector sensor are different during left lateral flexion due to the abnormal deformation of the body surface (Fig. 3i). In addition, the intensity of the corresponding signals generates discernible fluctuations under left and right lateral flexion as well as left and right rotation. These data indicate that the amplitude and direction of skin deformation on both sides are asymmetric under two sets of spinal motions. In moderate scoliosis patients, the thoracic Cobb angle is 26° (Fig. 3f). For severe scoliosis patients, the thoracic Cobb angle is 55°, and the lumbar Cobb angle is 34° (Fig. 3g). The 3D deformity of the spine induces significant alterations in body morphology. As the Cobb angle of the spine increases, the intensity difference in response signals corresponding to the three sets of symmetrical motions becomes more pronounced (Fig. 3j, k). For patients with severe scoliosis, left and right rotational motions may fail to induce skin deformation on the right side, resulting in weak response signals (Fig. 3k). During the study, we found that muscle tone has a limited practical impact on the proposed method, as detailed in Supplementary Note S7. In practical applications, temperature fluctuations did not cause noticeable drift in the response signals. Furthermore, we thoroughly considered the effects of human sweat, skin movement artifacts, and clothing friction on sensor performance, and adopted systematic engineering optimization strategies to minimize the impact of these factors (Supplementary Figs. S11d–f, S27 and Note S8).

Artificial intelligence-powered scoliosis identification

Analyzing the collected time series of signals from the 3D spinal morphology monitoring suit poses several challenges: the signals are multi-channel, encapsulating complex 3D spatial information; they are long-duration, with each signal containing information of three sets of symmetrical evaluation motions; and there is significant individual variability in the signals collected from different individuals. To address these challenges, as shown in Fig. 4a, we utilized Graph Convolutional Neural Networks (GCNNs) and developed a time-spatial modeling-based dynamic GCNN model named Graph-based Scoliosis Detection (GraphScoDetect). GraphScoDetect is further detailed in Supplementary Fig. S28, as well as in Supplementary Note S9 and S10. This model is adept at time-series node representation within dynamic spatial graphs. To prevent model overfitting, we introduced an inter-subject, self-supervised learning protocol during the pre-training phase, which allows the emergence of robust asymmetrical features. The detailed design of subject-wise positive and negative pair construction and the corresponding contrastive learning strategy are illustrated in Supplementary Fig. S29.

To rigorously evaluate GraphScoDetect, we recruited 145 scoliosis patients and 45 healthy controls from four hospitals and one school-based screening program, resulting in a total cohort of 190 participants. The average age of the scoliosis and control groups was 14.04 and 14.10 years, respectively ($P = 0.855$). Among the scoliosis patients, 53.1% presented with a single-curve pattern, 46.2% with a double-curve pattern, and 0.7% with a triple-curve pattern. Scoliosis severity was classified according to the Cobb angle and treatment strategy—measured from standardized standing posterior–anterior radiographs—into three clinically validated tiers: mild (10°–25°), moderate (25°–45°), and severe (>45°). Details of clinical cohort construction and the distribution of cohorts across participating centers are provided in Supplementary Note S11 and Supplementary Table S2, respectively.

To assess the generalization capability of GraphScoDetect, we performed subject-independent validation by strictly separating participants between training and testing sets. All repeated measurements acquired from the same participant were assigned to the same data split to avoid subject-level information leakage. Following a leave-one-subject-out (LOSO) evaluation protocol, each participant was iteratively used as an independent test subject while the remaining participants were used for model training. The details of subject-independent evaluation protocols are demonstrated in Supplementary Note S12. Under the LOSO protocol, GraphScoDetect achieved an accuracy of 92.63% (95% CI: 88.01–95.56%), a sensitivity of 96.55% (95% CI: 92.18–98.52%), and a specificity of 80.00% (95% CI: 66.18–89.10%) for binary scoliosis identification. The corresponding area under the receiver operating characteristic curve (AUROC) and the area under the precision–recall curve (AUPRC) were 95.03% (95% CI, 91.20–97.99%) and 98.24% (95% CI, 96.76–99.35%), respectively (Fig. 4b, c). Furthermore, additional subject-independent evaluations based on GroupKFold with different fold numbers and leave-one-center-out (LOCO) validation were conducted to further assess model robustness under different unseen-subject and unseen-center scenarios (Supplementary Tables S3 and S4). The corresponding confusion matrices under these validation protocols are provided in Supplementary Fig. S30. To ensure a fair comparison with existing methods, the selection criteria and implementation details of all baseline models are demonstrated in Supplementary Note S13 and Table S5. All baseline models were evaluated using the same preprocessing pipeline and subject-independent data partition strategy as GraphScoDetect. Under these consistent evaluation settings, GraphScoDetect achieved superior performance compared with existing baseline methods, demonstrating the effectiveness of the proposed multi-sensor graph-based representation learning framework for scoliosis identification.

To compare GraphScoDetect with conventional scoliosis screening protocols in a real-world screening scenario (Supplementary Fig. S31), we conducted an external-center evaluation using Zhejiang University Hospital as an unseen testing center. All participants in this cohort underwent conventional screening with FBT and scoliometer assessment, followed by whole-spine X-ray examination as the clinical reference standard. GraphScoDetect was trained using data from other centers and independently evaluated on the Zhejiang University Hospital cohort. In the external-center evaluation, GraphScoDetect achieved an accuracy of 87.72% (95% CI, 76.75–93.92%), a sensitivity of 92.86% (95% CI, 80.99–97.54%), and a specificity of 73.33% (95% CI, 48.05–89.10%; $N = 57$). The corresponding AUROC and AUPRC were 88.25% (95% CI, 76.98–96.83%) and 95.24% (95% CI, 90.53–98.87%), respectively (Fig. 4d, e; $N = 57$). The results demonstrate improved screening capability compared with conventional screening approaches and the potential to reduce unnecessary X-ray examinations.

To assess GraphScoDetect's capacity to discriminate scoliosis severity, we conducted a four-category classification task using the predefined clinical severity labels described above. To visualize the learned feature space, intermediate feature embeddings immediately before the classification head were extracted under leave-one-subject-out (LOSO) evaluation and projected into two dimensions using principal component analysis (PCA), implemented in scikit-learn. The phenotypic distributions exhibited distinct segregation (Fig. 4f), indicating that the features extracted by the trained model have obvious asymmetry characteristics. Under the LOSO validation protocol, GraphScoDetect achieved an accuracy of 71.05% (95% CI, 64.24–77.03%) and a balanced accuracy of 69.64% (95% CI, 62.29–76.80%) for four-category scoliosis severity classification (Fig. 4g). The area under the receiver operating characteristic curve (AUROC) and the area under the precision–recall curve (AUPRC) were 87.84% and 70.32%, respectively. Further analysis was then conducted to determine why one severe patient was misclassified as moderate in our approach. The patient has double curves, the thoracic curve with 36° and the lumbar curve with 55° (Supplementary Fig. S32). Given that the sensor is placed at the junction of thoracic and lumbar regions, the two curves were too close to distinguish the signals, ultimately resulting in misclassification.

https://doi.org/10.1038/s41467-026-79186-1

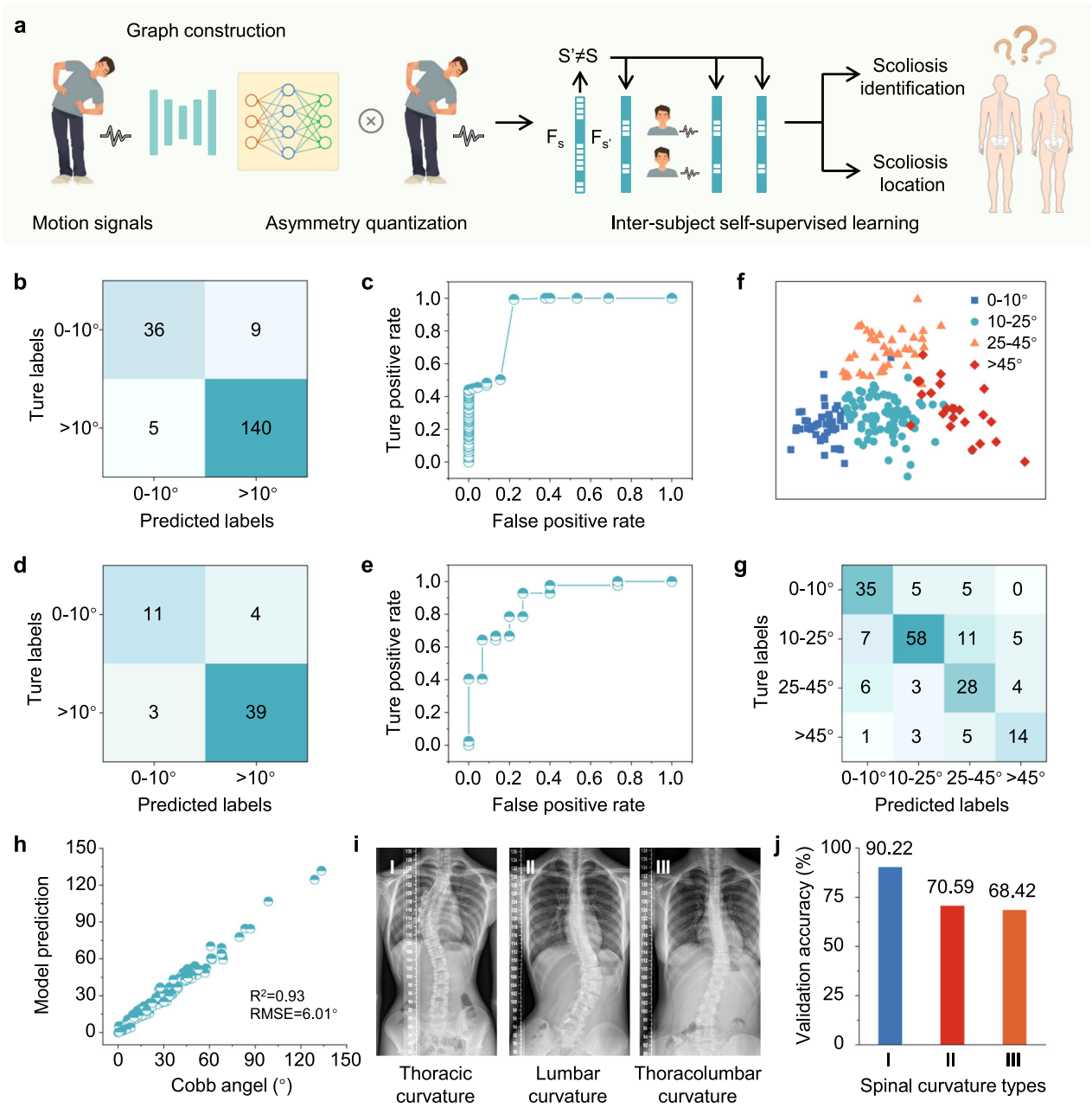


Fig. 4 | Artificial intelligence-powered scoliosis identification. a Overview of the Graph-based Scoliosis Detection (GraphScoDetect) framework, in which motion signals are processed to generate class probabilities and the class with the highest predicted probability is selected as the model output. Here, F_s and $F_{s'}$ denote the learned feature representation of the motion signals from subject S, where S is the subject index; $S' \neq S$ indicates that the paired feature representations originate from different subjects. **b** Confusion matrix for binary classification, reflecting the model's ability to differentiate scoliosis cases from non-scoliotic patients. **c** Receiver operating characteristic curve for binary scoliosis identification under leave-one-subject-out (LOSO) validation. **d** Confusion matrix for external-center binary scoliosis identification using participants from Zhejiang University Hospital as the independent test cohort ($N = 57$). **e** Receiver operating characteristic curves for the external-center evaluation. **f** Principal component analysis projection of the feature embeddings extracted before the classification head under LOSO validation. **g** Confusion matrix for four-category classification of normal, mild, moderate, and severe scoliosis under LOSO validation ($N = 190$). **h** Relationship between Cobb angles predicted by GraphScoDetect and those measured from radiographs by clinical experts. R^2 denotes the coefficient of determination, indicating the goodness of fit between the predicted and measured Cobb angles, whereas Root Mean Squared Error (RMSE) denotes the root mean square error, indicating the magnitude of the prediction error. **i** X-ray images of different types of spinal curvature, including thoracic curvature (I), lumbar curvature (II), and thoracolumbar curvature (III). **j** Class-wise recall for identifying thoracic, thoracolumbar, and lumbar curve locations among participants with scoliosis ($N = 145$).

We next evaluated whether the asymmetry-related features extracted by the GCNN could quantitatively map to the severity of scoliosis, represented by the clinically measured Cobb angle. For this purpose, we modified GraphScoDetect, replacing its final classification layer with a regression layer, specifically encompassing one long short-term memory layer and two linear layers. With this approach, GraphScoDetect achieved an Root Mean Squared Error (RMSE)of 6.01° (95% CI, 5.27–6.74°), an Mean Absolute Error (MAE) of 4.59° (95% CI, 4.04–5.15°), and a coefficient of determination (R^2) of 0.93 (Fig. 4h). Stratified analyzes showed MAE/RMSE values of 4.40°/5.35° for Cobb angles of 10–25°, 4.87°/6.12° for angles of >25–45°, and 8.19°/9.80° for angles >45°, respectively. This performance is comparable to the reported variability of manual Cobb angle measurements by clinicians[40,41], indicating the potential of the GCNN-based framework

for quantitative scoliosis assessment. The agreement between the wearable-based Cobb angle estimation and radiographic reference measurements was further evaluated using Bland–Altman analysis, demonstrating consistent agreement across the cohort (Supplementary Fig. S33).

We investigated the effects of sensor placement deviations and sensor-position ablation under subject-independent evaluation to assess the robustness and sensor contribution of GraphScoDetect. As summarized in Supplementary Table S6, GraphScoDetect maintained stable scoliosis identification performance under 18 sensor displacement conditions, including horizontal and vertical shifts with different displacement magnitudes. Although sensor displacement reduced waveform similarity, the learned feature representations remained relatively stable under most displacement conditions, as indicated by the Pearson correlation coefficient (PCC) and the relatively small feature distances. In contrast, large horizontal displacement of all sensors substantially altered the acquired motion patterns and increased the feature distance, leading to a decrease in identification accuracy to 60%. These results indicate that GraphScoDetect does not depend solely on precise sensor placement; rather, it learns robust representations of spinal motion asymmetry—capable of tolerating practical variations during real-world wearable deployment.

We further performed systematic sensor ablation analyzes to evaluate the contribution of different sensing configurations (Note S14 and Supplementary Tables S7–S13). Removing individual sensors consistently degraded performance, demonstrating the complementary roles of multiple sensing positions. Among all sensors, removing Sensor 3 caused the largest performance reduction in both binary identification and four-category severity classification, with accuracy decreases of 6.84% and 15.26%, respectively. Stratified analysis across different curvature locations further confirmed the dominant contribution of Sensor 3, particularly for thoracic, lumbar, and thoracolumbar curves (Supplementary Table S13). In addition, reducing the number of sensors resulted in progressive performance degradation, with the complete four-sensor configuration achieving the best overall performance (Supplementary Tables S9 and S10). Comparison among different sensing modalities further demonstrated that the combined configuration integrating uniaxial deformation and motion-vector information consistently outperformed single-modality designs, indicating complementary biomechanical representations of amplitude-sensitive and direction-aware spinal motion (Supplementary Tables S11 and S12).

During the screening and monitoring of scoliosis, we regard the spine as a whole to identify the presence and severity of disease, focusing on the most severe curve in cases of multi-curvature. We further investigated whether it was possible to identify the location of the curvature. Figure 4i exhibits the X-ray images of different types of spinal curvature, including thoracic curvature (I), lumbar curvature (II), and thoracolumbar curvature (III). To this end, we collected the signals on the trans-crossing plane between the chest and the abdomen, thereby theoretically assessing signals from thoracic, thoracolumbar, and lumbar curvature. GraphScoDetect achieved an overall curvature-location accuracy of 82.76% (95% CI, 75.79–88.04%), with class-wise recalls of 90.22% (95% CI, 82.44–94.77%) for thoracic curves, 68.42% (95% CI, 46.01–84.64%) for thoracolumbar curves, and 70.59% (95% CI, 53.83–83.17%) for lumbar curves (Fig. 4j). Compared with the conventional methods for scoliosis identification, the developed 3D spinal morphology monitoring suit can accurately identify the degree and location of scoliosis, providing a radiation-free alternative for scoliosis screening and potentially supporting longitudinal follow-up during the management of this condition (Supplementary Note S15 and Table S14).

Discussion

In this study, a 3D spinal morphology monitoring suit with embedded motion sensors is integrated to enable real-time tracking of 3D spinal motions by precisely detecting the amplitude and direction of skin deformation. Dynamic scoliosis identification is achieved by assessing the symmetry of human postures during symmetrical 3D spinal motions. Crucially, we utilized data from four medical centers and one school-based screening program to overcome the single-source bias. We developed a pioneering self-learning GCNN architecture to transform complex signal features into quantifiable patient asymmetry measures, which encodes and contrasts multiple data samples from different domains.

Under subject-independent validation, our method achieved robust performance for binary scoliosis screening and demonstrated the feasibility of severity classification based on wearable motion signals. The use of complementary evaluation metrics, including balanced accuracy, AUROC, and AUPRC for severity classification, provided a comprehensive assessment under imbalanced severity categories. Balanced accuracy reflects overall performance while accounting for category imbalance, AUROC characterizes discrimination capability across decision thresholds, and AUPRC provides additional evaluation of performance in imbalanced classification scenarios. Sensitivity and specificity further characterized the clinical screening capability by quantifying case detection and correct exclusion of non-scoliosis participants, respectively. We further identified the curvature positions of the spine, achieving an overall accuracy of 82.76%, with accuracies of 90.22% for thoracic curves, 68.42% for thoracolumbar curves, and 70.59% for lumbar curves.

Several limitations should be acknowledged. The cohort comprises 190 participants from five centers, of whom 45 are controls, so specificity estimates carry wide confidence intervals, and the four-category severity results, based on few severe (>45°) cases, should be regarded as exploratory. Control participants recruited through the school-based program did not undergo radiography for ethical reasons, and a small number of very mild curves may therefore have been classified as controls. The method also requires participants to execute three sets of symmetrical spinal motions, and each was assessed at a single supervised session; performance in individuals with restricted spinal mobility, across the mixed aetiologies represented in the cohort, and during unsupervised long-term wear therefore remains to be established. Prospective multi-center studies with paired radiographic follow-up are under way.

This work provides a viable alternative for radiation-free scoliosis screening, with the potential to support longitudinal follow-up and to reduce the number of repeat radiographs required during the management of the condition.

Methods

Materials

PU powders with a molecular weight of 200,000 g/mol were supplied by BASF Polyurethane Specialties (Guangdong, China). The purity level of the PU exceeded 99.9%. A water-based dispersion of carbon nanotubes (CNTs), featuring an average diameter of 50 nm, was obtained from Nanjing XFNANO Materials Tech Co., Ltd. (Jiangsu, China). The concentration of CNTs in the dispersion was 10 wt%. N,N-Dimethylformamide (DMF) and tetrahydrofuran (THF), both of analytical grade (purity ≥99.9%), were purchased from Aladdin Reagent Database Co., Ltd. (Shanghai, China).

Preparation of the PU meshes with different fiber orientations

PU powders were dissolved in a mixed solvent of DMF and THF at a mass ratio of 2:3 to prepare a 20 wt% polymer solution, which was magnetically stirred for 8 h at 60 °C. Electrospinning was carried out using a NANON electrospinning system (MECC Co., Ltd.) under the following optimized parameters, including an applied voltage of 20 kV,

a syringe pump flow rate of 0.5 mL h^{-1}, and collector rotational speeds of 200 and 2000 rpm. The collector, which was covered with aluminum foil, was positioned 20 cm from the injector nozzle. The ambient temperature and relative humidity were maintained at 25 °C and 25%, respectively. The electrospinning duration was 8 h per sample. Subsequently, the PU meshes were dried under vacuum at 60 °C for 6 h to remove residual solvents.

Preparation of the CNTs@PU meshes with different fiber orientations

Samples of the PU mesh, based on unidirectional and unordered fibers, were prepared separately. Subsequently, each mesh was immersed in the aqueous CNT dispersion and subjected to ultrasonication for 30 min at ambient temperature to promote uniform CNT adsorption. Excess dispersion was gently blotted from the mesh surface, after which the samples were wound onto a polytetrafluoroethylene (PTFE) substrate and dried under vacuum at 60 °C for 6 h. Finally, the CNTs@PU meshes were carefully peeled off the PTFE substrate.

Construction of the uniaxial motion sensor and motion vector sensor

The isotropic PU mesh based on unordered fibers served as both the encapsulation layer and the insulation layer, while the anisotropic CNTs@PU mesh based on unidirectionally aligned fibers functioned as the sensitive layer. Different functional layers were patterned using a laser engraving machine (LaserMen, LM-6040) under controlled conditions: laser power of 10 W and scanning speed of 100 mm/s. In the uniaxial motion sensor, the prepared encapsulation layer is rectangular in shape, with side lengths of 5.4 × 1.4 cm; the prepared strain-sensitive layer is also rectangular in shape, with a size of 5 × 1 cm, and an additional electrical interface needs to be reserved. In the motion vector sensor, the prepared encapsulation layer and insulation layer were circular, with diameters of 4 cm and 3.6 cm, respectively; the prepared strain-sensitive layer is strip-shaped, with a size of 5.2 × 0.5 cm. By sandwiching two isotropic encapsulation layers with an anisotropic sensitive layer, the uniaxial motion sensor was constructed by the hot-pressing process. By sequentially stacking the bottom encapsulating layer, bottom strip-like sensitive layer, insulating layer, top strip-like sensitive layer, and top encapsulating layer from bottom to top, the motion vector sensor was fabricated by the hot-pressing process. The optimal parameters for the hot-pressing process were as follows: an applied pressure of 10 MPa, a temperature of 60 °C, and a dwell time of 30 s.

Integration of the 3D spinal morphology monitoring suit

In this study, the elastic bodysuit serves as an integrated substrate for motion sensors, conductive wires, and FPCBs. To facilitate integration, we developed a custom ironing adhesive patch. One side of the patch is coated with hot-melt adhesive, which ensures strong adhesion between the patch and the elastic bodysuit. The other side features a high-strength adhesive designed to provide robust bonding with each module. Subsequently, the various modules are integrated onto the elastic bodysuit using the ironing adhesive patch as the medium. After precisely positioning and placing the ironing adhesive patches on the elastic bodysuit, the patches are heated with an iron at 180 °C for 10 s, followed by a cooling period. Next, the motion sensors, conductive wires, and FPCB are accurately positioned and securely adhered to the elastic bodysuit. Finally, each module is encapsulated with a layer of elastic fabric to complete the packaging process.

Patients

All kinds of scoliosis, including idiopathic, congenital, neuromuscular, and syndromic scoliosis, have the same phenotypes as a curved spine, uneven shoulders, and asymmetry of the back, and the disease severity is determined by the Cobb angle. Etiology was recorded for every participant, and the cohort was deliberately pooled rather than stratified by etiology, because the method targets the scoliotic phenotype rather than a single etiological subtype. Our inclusion criteria are: 1) agree to participate in the study and sign the consent. 2) with confirmed or suspected scoliosis; Exclusion criteria are: 1) vertebral malformation; 2) cannot finish the test; 3) history of prior spinal surgery; 4) degenerative (adult de novo) scoliosis. Brace treatment was not an exclusion criterion, and brace treatment history was recorded as clinical metadata. Risser stage and menarche status were recorded as indicators of skeletal maturity but were not applied as inclusion criteria. The clinical trial included five cohorts: cohorts 1 to 3 were collected from three hospitals in clinical settings, and cohort 4 was also collected from one hospital for participants who were screened positively in a school screening program. Cohort 5 was recruited through a school-based screening program. For ethical reasons, radiography was not performed in asymptomatic screen-negative minors; the scoliosis-negative status of these participants was therefore established by three negative screening tests together with a confirmatory physical examination by a spine-deformity surgeon with more than ten years of subspecialty experience, rather than by radiography. This difference in reference standard between Cohort 5 and Cohorts 1–4 is acknowledged in the Limitations.

Radiography and disease severity

All patients testing positive on any preliminary screening method, such as the FBT or scoliometer assessment, were referred to a surgeon for radiological verification and additional evaluations. In datasets 1–4, sourced from various medical centers, participants underwent an anteroposterior standing full-length spinal X-ray to confirm the presence of scoliosis. The Cobb angle, a critical measure of spinal curvature, was independently assessed by the same two experienced spine surgeons for all participants across all five centers, so that annotation was not confounded by center-specific reading practice. Both readers were blinded to the wearable sensor results, and any discrepancy between the two readings was resolved by consensus discussion. Disease management was stratified based on the Cobb angle measurements: 1) Normal: no treatment required for Cobb angles less than 10 degrees; 2) Close Monitoring: Cobb angles between 10 and 25 degrees; 3) Brace Treatment: Cobb angles between 25 and 45 degrees; 4) Surgical Intervention: Cobb angles exceeding 45 degrees.

Model evaluation and statistical analysis

All model evaluations were performed under subject-independent protocols. Specifically, repeated measurements from the same participant were assigned exclusively to the same data partition to prevent information leakage. GraphScoDetect was evaluated using leave-one-subject-out (LOSO), GroupKFold with 3, 5, 7, and 10 folds, and leave-one-center-out (LOCO) validation. In GroupKFold settings, participants were divided into folds while keeping all measurements from the same participant within the same fold. LOCO validation was conducted by holding out one recruitment center as an independent test set. All baseline models were implemented using the same preprocessing pipeline and subject-level partition strategy. Experiments were repeated with multiple random seeds, and results were reported as mean ± standard deviation when applicable. Performance was evaluated using task-specific classification metrics. Confidence intervals for classification proportions were calculated using the Wilson method, while confidence intervals for AUROC were estimated using bootstrap resampling. Model training and statistical analyzes were implemented in Python 3.10 using PyTorch 2.2.1, scikit-learn 1.4.2, NumPy 1.26.4, and SciPy 1.12.0.

Characterization

Surface morphologies of all fabricated materials and sensors were examined by field-emission scanning electron microscopy (FEI, Quanta

3D FEG). Mechanical properties were evaluated using a universal tensile testing system (Mark-10 ESM303) under a controlled displacement rate and ambient conditions. For electromechanical characterization, the CNT@PU meshes and the sensors were subjected to tensile loading on the same Mark-10 ESM303 system, while real-time resistance changes were simultaneously recorded using a high-precision digital multimeter (Keithley DMM7510).

Ethics oversight

All procedures involving human research participants were conducted in accordance with the experimental protocol approved by the Ethics Committee on the Use of Humans as Experimental Subjects of the Peking Union Medical College Hospital, Peking Union Medical College and Chinese Academy of Medical Sciences (No. I-24PJ0473). All participants or their parents/legally authorized representatives were informed and provided written consent. Permission has been obtained to publish images and information that identify individuals.

Reporting summary

Further information on research design is available in the Nature Portfolio Reporting Summary linked to this article.

Data availability

The data generated in this study are provided in the Supplementary Information/Source Data file. Example wearable-sensor data and the implementation code for GraphScoDetect are publicly available at https://github.com/DhrLhj/GraphScoDetect. The raw datasets generated in this study are protected and are not publicly available due to participant privacy and ethical restrictions concerning sensitive clinical information. Data access and any additional requests can be obtained by submitting a specific research proposal and signing a Data Transfer Agreement with the corresponding author (yuezhang@ustb.edu.cn). Data sharing is restricted to academic researchers for non-commercial purposes. We will respond to requests within two weeks, and access is granted for a 2-year authorization period. Any additional requests for information can be directed to, and will be fulfilled by, the corresponding authors. Source data are provided with this paper.

Code availability

The Python code (Python 3.10 +) for the GraphScoDetect model and associated analyzes is publicly available at https://github.com/DhrLhj/GraphScoDetect. The version of the code associated with this study is archived on Zenodo at https://doi.org/10.5281/zenodo.23276628[42].

References

1. Cheng, J. C. et al. Adolescent idiopathic scoliosis. *Nat. Rev. Dis. Prim.* **1**, 15030 (2015).
2. Weinstein, S. L. et al. Health and function of patients with untreated idiopathic scoliosis: a 50-year natural history study. *JAMA* **289**, 559–567 (2003).
3. Weinstein, S. L. et al. Curve progression in idiopathic scoliosis. *J. Bone Jt. Surg. Am.* **65**, 447–455 (1983).
4. Addai, D. et al. Current concepts in the diagnosis and management of adolescent idiopathic scoliosis. *Childs Nerv. Syst.* **36**, 1111–1119 (2020).
5. Helenius, L. et al. Back pain and quality of life after surgical treatment for adolescent idiopathic scoliosis at 5-year follow-up: comparison with healthy controls and patients with untreated idiopathic scoliosis. *J. Bone Jt. Surg. Am.* **101**, 1460–1466 (2019).
6. Diarbakerli, E. et al. Health-related quality of life in adulthood in untreated and treated individuals with adolescent or juvenile idiopathic scoliosis. *J. Bone Jt. Surg. Am.* **100**, 811–817 (2018).
7. Negrini, S. et al. 2016 SOSORT guidelines: orthopedic and rehabilitation treatment of idiopathic scoliosis during growth. *Scoliosis Spinal Disord.* **13**, 3 (2018).
8. Weinstein, S. L. et al. Effects of bracing in adolescents with idiopathic scoliosis. *N. Engl. J. Med.* **369**, 1512–1521 (2013).
9. Grossman, D. C. et al. Screening for adolescent idiopathic scoliosis: US Preventive Services Task Force recommendation statement. *JAMA* **319**, 165–172 (2018).
10. Fong, D. Y. T. et al. A meta-analysis of the clinical effectiveness of school scoliosis screening. *Spine* **35**, 1061–1071 (2010).
11. Lee, C. F. et al. Referral criteria for school scoliosis screening: assessment and recommendations based on a large longitudinally followed cohort. *Spine (Philos. Pa 1976)* **35**, E1492–E1498 (2010).
12. Yawn, B. P. et al. A population-based study of school scoliosis screening. *JAMA* **282**, 1427–1432 (1999).
13. Fong, D. Y. et al. A population-based cohort study of 394,401 children followed for 10 years exhibits sustained effectiveness of scoliosis screening. *Spine J.* **15**, 825–833 (2015).
14. Karachalios, T. et al. Ten-year follow-up evaluation of a school screening program for scoliosis. Is the forward-bending test an accurate diagnostic criterion for the screening of scoliosis? *Spine (Philos. Pa 1976)* **24**, 2318–2324 (1999).
15. Dunn, J. et al. Screening for Adolescent Idiopathic Scoliosis: Evidence Report and Systematic Review for the US Preventive Services Task Force. *JAMA* **319**, 173–187 (2018).
16. Galbusera, F. et al. The spine: a strong, stable, and flexible structure with biomimetic potential. *Biomimetics* **4**, 60 (2019).
17. D'Amico, M. et al. A self-contained 3D biomechanical analysis lab for complete automatic spine and full skeleton assessment of posture, gait and run. *Sensors* **21**, 3930 (2021).
18. Eyvazov, K. et al. The association of lumbar curve magnitude and spinal range of motion in adolescent idiopathic scoliosis: a cross-sectional study. *BMC Musculoskelet. Disord.* **18**, 51 (2017).
19. Lee, Y. et al. Visual-inertial hand motion tracking with robustness against occlusion, interference, and contact. *Sci. Robot.* **6**, eabe1315 (2021).
20. Kidziński, Ł et al. Deep neural networks enable quantitative movement analysis using single-camera videos. *Nat. Commun.* **11**, 4054 (2020).
21. Kadirvelu, B. et al. A wearable motion capture suit and machine learning predict disease progression in Friedreich's ataxia. *Nat. Med.* **29**, 86–94 (2023).
22. Ricotti, V. et al. Wearable full-body motion tracking of activities of daily living predicts disease trajectory in Duchenne muscular dystrophy. *Nat. Med.* **29**, 95–103 (2023).
23. Yoon, H. et al. Decoding tissue biomechanics using conformable electronic devices. *Nat. Rev. Mater.* **10**, 4–27 (2025).
24. Tashakori, A. et al. Capturing complex hand movements and object interactions using machine learning-powered stretchable smart textile gloves. *Nat. Mac. Intell.* **6**, 106–118 (2024).
25. Park, M. et al. Stretchable glove for accurate and robust hand pose reconstruction based on comprehensive motion data. *Nat. Commun.* **15**, 5821 (2024).
26. Gong, R. et al. Stretchable sensors for detection of complex deformations. *Natl. Sci. Open.* **5**, 20260011 (2026).
27. Araromi, O. A. et al. Ultra-sensitive and resilient compliant strain gauges for soft machines. *Nature* **587**, 219–224 (2020).
28. Li, C. et al. Sensing of joint and spinal bending or stretching via a retractable and wearable badge reel. *Nat. Commun.* **12**, 2950 (2021).
29. Yang, H. et al. Topographic design in wearable MXene sensors with in-sensor machine learning for full-body avatar reconstruction. *Nat. Commun.* **13**, 5311 (2022).
30. Fan, S. et al. Strain-sensitive thermochromic smart electronic skin for joint and spine healthcare applications. *Adv. Sci.* **12**, e07605 (2025).

31. Cheng, A. et al. An intelligent hybrid-fabric wristband system enabled by thermal encapsulation for ergonomic human-machine interaction. *Nat. Commun.* **16**, 591 (2025).
32. Hong, Y. et al. Highly anisotropic and flexible piezoceramic kirigami for preventing joint disorders. *Sci. Adv.* **7**, eabf0795 (2021).
33. Lee, J. H. et al. Heterogeneous structure omnidirectional strain sensor arrays with cognitively learned neural networks. *Adv. Mater.* **35**, e2208184 (2023).
34. Yin, H. et al. Ultra-high sensitivity anisotropic piezoelectric sensors for structural health monitoring and robotic perception. *Nano-Micro Lett.* **17**, 42 (2025).
35. Ketelsen, B. et al. Nanoparticle-based strain gauges: anisotropic response characteristics, multidirectional strain sensing, and novel approaches to healthcare applications. *Adv. Funct. Mater.* **33**, 2210065 (2023).
36. Wang, X. et al. A highly stretchable transparent self-powered triboelectric tactile sensor with metallized nanofibers for wearable electronics. *Adv. Mater.* **30**, 1706738 (2018).
37. Kim, K. K. et al. Highly sensitive and stretchable multidimensional strain sensor with prestrained anisotropic metal nanowire percolation networks. *Nano. Lett.* **15**, 5240–5247 (2015).
38. Zhang, H. et al. Anisotropic, wrinkled, and crack-bridging structure for ultrasensitive, highly selective multidirectional strain sensors. *Nano-Micro Lett.* **13**, 122 (2021).
39. Jiang, C. et al. Multiscale interconnected and anisotropic morphology genetic piezoceramic skeleton-based flexible self-powered 3D force sensor. *Adv. Funct. Mater.* **35**, 2503120 (2025).
40. Morrissy, R. T. et al. Measurement of the Cobb angle on radiographs of patients who have scoliosis. Evaluation of intrinsic error. *J. Bone Jt. Surg. Am.* **72**, 320–327 (1990).
41. Gstoettner, M. et al. Inter- and intraobserver reliability assessment of the Cobb angle: manual versus digital measurement tools. *Eur. Spine J.* **16**, 1587–1592 (2007).
42. Liu, H. et al. A motion vector sensor-enabled 3D spinal morphology monitoring suit for intelligent scoliosis identification: GraphSco-Detect v5.0.0 reproducibility code. *Zenodo* https://doi.org/10.5281/zenodo.23276628 (2026).

Acknowledgments

We thank the participating patients and their families for their contribution to this study. This work was supported by the High Performance Computing Cluster of the Center for Bioinformatics, National Infrastructures for Translational Medicine (Peking Union Medical College Hospital), through computing resources and technical services. We thank the software tools such as Blender, Krita and Microsoft PowerPoint for providing strong support for the 3D modeling, image drawing and figure layout of this work.

Author contributions

L.X., G.C., H.L., X.Z., T.J.Z., Q.L., Y.Z., and N.W. conceived the idea and designed the research. L.X. and X.Z. prepared the materials, constructed the uniaxial and biaxial strain sensors, and integrated the sensing suit. L.X. and H.S. carried out the characterization of the materials and measurement of the sensors. L.X., G.C., and H.L. collected multi-center data. M.L., Y.W., B.W., X.Y., and J.Y. assisted in multi-center data collection. H.L. and C.Y. performed scoliosis identification by machine learning. G.Q. and Z.W. provided guidance in the methodology. L.X., G.C., H.L., X.Z., Q.L., Y.Z., and N.W. co-wrote the manuscript. All authors discussed the results and commented on the manuscript.

Funding

This work was supported by the National Natural Science Foundation of China under Grant Nos. 52188101 (Y.Z.), 52232006 (Q.L.), U25A20236 (Q.L.), 52372133(X.Z.), 52502162 (L.X.), 62332017 (C.Y.), and 82572698 (J.Z.), CAMS Innovation Fund for Medical Sciences under Grant Nos. 2024-I2M-TS-002 (N.W.), 2025-I2M-XHJC-002 (N.W.), 2026-I2M-SXZX5-03 (J.Z.), National High Level Hospital Clinical Research Funding under Grant Nos.2025-PUMCH-C-003 (J.Z.), Peking Union Medical College Hospital Talent Cultivation Program (Category A) under Grant Nos. ULJ11240 (N.W.), China Postdoctoral Science Foundation under Grant Nos. 2025M770166 (L.X.), 2026T190007 (L.X.), and Postdoctoral Fellowship Program of CPSF under Grant Nos. GZC20250113 (L.X.). The Huadong Medicine Joint Funds of the Zhejiang Provincial Natural Science Foundation of China under Grant Nos. HDMY23H100021 (M.L.).

Competing interests

The authors declare no competing interests.

Additional information

Supplementary information The online version contains supplementary material available at https://doi.org/10.1038/s41467-026-79186-1.

Correspondence and requests for materials should be addressed to Terry Jianguo Zhang, Qingliang Liao, Yue Zhang or Nan Wu.

Peer review information *Nature Communications* thanks Hongfei Wang, Weili Deng and the other anonymous reviewer for their contribution to the peer review of this work. A peer review file is available.

Reprints and permissions information is available at http://www.nature.com/reprints

Publisher's note Springer Nature remains neutral with regard to jurisdictional claims in published maps and institutional affiliations.

Open Access This article is licensed under a Creative Commons Attribution-NonCommercial-NoDerivatives 4.0 International License, which permits any non-commercial use, sharing, distribution and reproduction in any medium or format, as long as you give appropriate credit to the original author(s) and the source, provide a link to the Creative Commons licence, and indicate if you modified the licensed material. You do not have permission under this licence to share adapted material derived from this article or parts of it. The images or other third party material in this article are included in the article's Creative Commons licence, unless indicated otherwise in a credit line to the material. If material is not included in the article's Creative Commons licence and your intended use is not permitted by statutory regulation or exceeds the permitted use, you will need to obtain permission directly from the copyright holder. To view a copy of this licence, visit http://creativecommons.org/licenses/by-nc-nd/4.0/.

© The Author(s) 2026

This Article in Press is shared early to give you faster access to new research. It is citable and carries a permanent DOI. The final edited version will replace it automatically.

[1]Academy for Advanced Interdisciplinary Science and Technology, Key Laboratory of Advanced Materials and Devices for Post-Moore Chips, Ministry of Education, University of Science and Technology Beijing, Beijing, People's Republic of China. [2]Beijing Key Laboratory of Two-Dimensional Semiconductors for Future Chips, School of Materials Science and Engineering, University of Science and Technology Beijing, Beijing, People's Republic of China. [3]State Key

Laboratory for Advanced Metals and Materials, University of Science and Technology Beijing, Beijing, People's Republic of China. [4]Department of Orthopedic Surgery, State Key Laboratory of Complex Severe and Rare Diseases, Peking Union Medical College Hospital, Peking Union Medical College and Chinese Academy of Medical Sciences, Beijing, People's Republic of China. [5]Beijing Key Laboratory of Big Data Innovation and Application for Skeletal Health Medical Care, Key Laboratory of Big Data for Spinal Deformities, Peking Union Medical College Hospital, Peking Union Medical College and Chinese Academy of Medical Sciences, Beijing, People's Republic of China. [6]School of Intelligence Science and Technology, University of Science and Technology Beijing, Beijing, People's Republic of China. [7]Department of Orthopedic Surgery, The First Affiliated Hospital, Zhejiang University School of Medicine (FAHZU), Hangzhou, Zhejiang, People's Republic of China. [8]Peking University First Hospital, Beijing, People's Republic of China. [9]Weifang People's Hospital, Shandong (The First Affiliated Hospital of Shandong Second Medical University), Qingdao, Shandong, People's Republic of China. [10]School of Biomedical Engineering, School of Ophthalmology and Optometry and Eye Hospital, Wenzhou Medical University, Hangzhou, Zhejiang, People's Republic of China. [11]These authors contributed equally: Liangxu Xu, Guilin Chen, Hongjun Liu, Xuan Zhao. jgzhang_pumch@yahoo.com; liao@ustb.edu.cn; yuezhang@ustb.edu.cn; dr.wu-nan@pumch.cn